Steady and oscillatory flow in the human bronchial tree

Sahar Jalal,[*] Tristan Van de Moortele,[†] Omid Amili,[‡] and Filippo Coletti
Department of Aerospace Engineering & Mechanics, University of Minnesota, Minneapolis, Minnesota 55455, USA

(Received 20 January 2020; accepted 29 May 2020; published 17 June 2020)

In this study, we investigate the steady inhalation, steady exhalation, and oscillatory flow in a realistic airway geometry for physiologically relevant regimes ranging from quiet breathing to respiration under high frequency ventilation (HFV). We use magnetic resonance velocimetry to characterize and quantify three-dimensional (3D) velocity fields in 3D printed replicas of realistic bronchial trees. Expanding on previous studies [Jalal *et al.*, Exp. Fluids **57**, 148 (2016); Jalal *et al.*, Phys. Rev. Fluids **3**, 103101 (2018)] which focused on respiration in planar double bifurcation geometries, we compare levels of axial and lateral dispersion, and find that they exceed those found in the idealized models. Furthermore, we find that the secondary flows in realistic airways propagate deep in the bronchial tree and are stronger during exhalation as compared to inhalation, while the mean flow topology does not vary significantly between the two steady regimes. Under HFV, we note significant regions of flow reversal during the inhalation-exhalation and exhalation-inhalation transitions. This is found to be due to a difference in impedance (dominated by inertance) in the different regions of the lung and results in an asynchronous ventilation between the upper and lower lobes. This phenomenon, also known as pendulluft is demonstrated experimentally for the first time, using both Eulerian velocity fields and Lagrangian pathlines. Secondary flows are stronger in exhalation compared to inhalation and at the peak of the ventilation cycle, match the steady cases although the flow topology can be significantly different. Finally, the cycle-averaged drift velocity suggests that steady streaming, while not negligible, is not the main transport mechanism during high-frequency ventilation.

DOI: 10.1103/PhysRevFluids.5.063101

I. INTRODUCTION

Respiratory diseases are among the leading causes of death worldwide, and unlike other major illnesses, their incidence keeps increasing [1,2]. On the other hand, aerosol drug delivery devices have low deposition efficiencies [3,4], which is symptomatic of an unsatisfactory understanding of the transport mechanisms within the human airways. Deepening our knowledge of the respiratory fluid dynamics is therefore imperative. Building on seminal work on simplified bifurcating branches [5–7], numerical and experimental methods have significantly advanced the field in the last decade [8–11]. Still, as discussed in Ref. [12], the vast majority of studies are restricted to the inhalation phase. While this might seem the more consequential, the exhalation phase also deserves attention due to its importance for, e.g., gas exchange, pressure drop, and inhaled particle transport [13].

[*]Present address: Department of Radiology, Weill Cornell Medicine and New York–Presbyterian Hospital, New York, New York 10021, USA.
[†]Present address: Cardiovascular Systems Inc., Saint Paul, Minnesota 55112, USA.
[‡]Present address: Department of Mechanical, Industrial, and Manufacturing Engineering, University of Toledo, Toledo, Ohio 43606, USA.

 ©2020 American Physical Society

Moreover, at high breathing rate, the oscillatory flow dynamics cannot be described by the mere alternation of steady inhalation and exhalation and become dominated by unsteady effects [14]. The latter are even more central in high frequency ventilation (HFV). This is a widespread technique of mechanical ventilatory support routinely used to treat acute lung injury (ALI), acute respiratory distress syndrome (ARDS), and severe acute respiratory syndrome (SARS). It uses higher-than-normal breathing frequencies and low tidal volumes [15]. Despite its importance and common use, the performance of this approach in terms of gas exchange remain incompletely understood [16].

Besides the flow regime, the airway anatomy is believed to play a key role in determining the gas exchange and the fate of inhaled particles in the lungs. Therefore, while idealized airwaylike models have fruitfully been used to explore fundamental aspects of respiratory fluid mechanics, the transport in anatomically accurate airways may be substantially different. Computational methods have been increasingly used to simulate the flows in human airways. The needed experimental validation, however, is often lacking due to major practical difficulties. If *in vivo* measurements of air flow fields in the lungs are extremely challenging and offer limited spatial resolution, *in vitro* velocimetry in realistic replicas of the bronchial tree are also arduous due to geometrical complexities. Laser imaging in this type of physical models (usually based on computed tomography scans) has mostly been carried out either on two-dimensional (2D) planes [17] or in 3D volumes encompassing limited portions of the main bronchi [18,19]. Using magnetic resonance imaging, Banko and co-workers [20,21] successfully measured the full volumetric 3D flow of a realistic airway model down to the seventh generation of bronchial branching, although they imposed simplistic boundary conditions in terms of lobar ventilation rates.

Considering the above, in the present study we investigate the respiratory fluid flow in a realistic bronchial tree extending from the trachea to subsegmental (sixth-to-seventh) generations of bronchial branching. We leverage high-resolution medical imaging and 3D printing to create a precise replica of a subject-specific anatomy, impose subject-specific boundary conditions, and use magnetic resonance velocimetry (MRV) [22,23] to acquire volumetric velocity fields in a range of physiological flow conditions. In particular we focus on steady inhalation, steady exhalation, and high frequency ventilation. Steady conditions are physiologically important, as respiratory flow can be quasisteady during normal breathing [24,25]; they are also directly relevant to deep-breath inhalation maneuvers in aerosol drug delivery. High frequency ventilation, on the other hand, is characterized by specific flow features and transport mechanisms [14,26]. We evaluate various transport mechanisms and explicitly compare our results with recent studies performed in idealized models [12,27], highlighting similarities and differences. The paper is organized as follows: in Sec. II we introduce the methodology for the creation of the airway model, briefly describe the MRV methodology, and define the considered regimes; in Sec. III we present the results for steady inhalation, steady exhalation, and HFV; in Sec. IV we draw conclusions.

II. METHODS: AIRWAY MODEL, MRV MEASUREMENTS, AND FLOW REGIMES

We consider a female subject (1.58 m and 79 kg, body-mass index of 31.45) with no smoking history and healthy lung function. Chest scans were acquired as part of the COPDGene® study [28] using multidetector computer tomography (MDCT) that resulted in a mean isotropic voxel size of $0.3\,\mathrm{mm}^3$ [29]. Scans are available both at full inhalation (total lung capacity, TLC) and at full exhalation (functional residual capacity, FRC). We segment the five lobes [right upper lobe (RUL), right middle lobe (RML), right lower lobe (RLL), left upper lobe (LUL), and left lower lobe (LLL)] at both TLC and FRC. This allows us to quantify the subject-specific ventilation ratios, i.e., the fractions of inhaled air directed to each lobe. These are listed in Table I, and are consistent with previously reported values [30,31]. The model does not include the extra-thoracic airways. While those may have significant impact on the downstream flow [32], focusing on the bronchial tree allows us to isolate transport mechanisms through the bifurcating branches, which are relevant to the phenomenology of prevalent airway diseases such as asthma and chronic bronchitis.

TABLE I. Ventilation fraction across the five lobes of the considered subject: right upper lobe (RUL), right middle lobe (RML), right lower lobe (RLL), left upper lobe (LUL), and left lower lobe (LLL).

	RUL	RML	RLL	LUL	LLL
Ventilation fraction (%)	14	5	32	17	32

The experimental methodology to build the physical model is described in detail in Refs. [33,34], and is summarized here for completeness. We use the TLC scan to reconstruct the bronchial tree from the trachea to the seventh generation of bronchial branching (in average), and the tree centerline is extracted via a semiautomatic skeletonization process. The bronchial branches belonging to each lobe are highlighted in Fig. 1. The centerline from the skeletonization process defines the branching points in the airway tree. A consistent definition of the airway branch is needed. Considering the distance between successive bifurcation points along the airway tree, the central 50% of such distance is conventionally considered as the branch distinguished from the bifurcation regions. This type of definition is used in lung morphometry studies to define the branch length [35,36] and we have used it recently in a study where we coupled lung morphometry and respiratory fluid dynamics using an approach analogous to the present one [43]. The process of segmentation (i.e., the reconstruction of the airway geometry from the MDCT intensity matrix) is subject to inherent uncertainty. Here we use the commercial software MIMICS (Materialise Inc., Belgium) which has been shown via phantom-based validation to return accurate geometries, with errors much smaller than the native spatial resolution [37]. The software applies a weighted Laplacian smoothing algorithm to filter spurious edges caused by the limited spatial resolution. The reconstructed airways are used to generate a life-size hollow model. This is fitted in a vessel partitioned into five cavities, each collecting the distal bronchi of the respective lobe. The vessel and the airway tree are 3D-printed in one piece by stereolithography using WaterShed XC 11122, with a resolution of 100 μm at the W.M. Keck Center (University of Texas El Paso, TX). The actual wall roughness on the internal surface of the airways could not be directly measured but it is expected to be much smaller than the nominal resolution, because the final steps in stereolithography

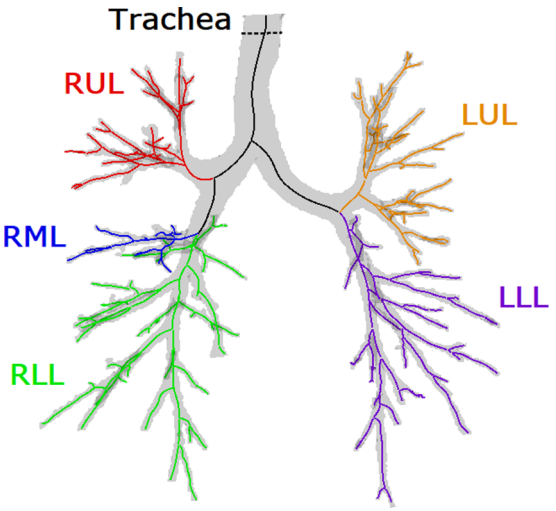

FIG. 1. Silhouette of the considered bronchial tree segmented from MDCT chest scan of a healthy subject, with branches grouped by lobe. The tracheal cross section where the bulk velocity U_0 and hydraulic diameter D_0 are defined (marked with a dashed line) is $3D_0$ above the carina.

postprocessing (using abrasive techniques) smoothen the surface and greatly alleviate the staircase effect [38]. Thus, at the present range of Reynolds number, the airway surface is expected to be hydrodynamically smooth. The above is supported by numerous previous studies, including the comparison between the measurements of Cherry *et al.* [39] (using a methodology similar to ours) and the direct numerical simulations of Ohlsson *et al.* [40] who found excellent agreement in their study of a separated diffuser designed to be very sensitive to geometric variations. In using a rigid model based on a TLC scan for both inhalation and exhalation, we neglect the change in airway geometry during respiration. This is appropriate when investigating the central airways, due to their limited motion and small change in cross section during the breathing cycle [8].

The model is inserted in a flow loop circulating water doped with 0.06 mol/L of $CuSO_4$, with plastic tubing connecting the trachea to a pumping system and the five lobes to a holding tank. For the steady inhalation and steady exhalation cases we use a centrifugal pump attached to a digital flow regulator (for details, see Ref. [27]), while for the oscillatory flow case we use a computer-controlled piston pump (described in Ref. [41]). The outlets of the lobar plena are each provided with needle valves and monitored via a clamp-on ultrasonic flow meter. For the steady flow cases, each lobar flow rate is adjusted to match the ventilation ratios in Table I. The same valve settings are used for the oscillatory cases, which results in close agreement (within a few percent) with the same ratios at peak inhalation and peak exhalation. During the inversion phases (inhalation-exhalation and exhalation-inhalation), the lobar flow distribution changes significantly due to the impedance of the different segments in the bronchial tree, as we shall discuss in the Results section.

In the MRV measurements the model is lodged in a 20-channel head coil connected to a 3T MRI scanner. Three-dimensional, three-component velocities are obtained on a Cartesian grid at an isotropic resolution of 0.6 mm. Those are either time-averaged (steady cases) or phase-averaged (oscillatory cases), as described in Refs. [12,27], where the acquisition and processing procedures are detailed. The time-average nature of MRV precludes the observations of instantaneous flow features and Reynolds stresses; these are influential for momentum transport, gas exchange, and deposition of inhaled particles [42]. Therefore, this represents a limitation of the present approach. We use encoding velocity $V_{\text{enc}} = 0.60\,\text{m/s}$ for all cases at nominal $\text{Re} = 1500$, while we use $V_{\text{enc}} = 0.75\,\text{m/s}$ for the case at $\text{Re} = 4500$. V_{enc} is kept the same in all three directions. The average signal-to-noise ratio SNR = 43.6 and 46.8 for the steady and oscillatory cases, respectively. In all cases, four scans are averaged to increase the signal-to-noise ratio, resulting in uncertainties of 5.5% (10.6%) of the bulk flow velocity (peak inhalation bulk velocity) at the trachea in the steady (oscillatory) case. For the oscillatory case, the wave-form period corresponding to one breathing cycle is divided into 15 phases, and a velocity field is reconstructed for each of them. The piston pump generates a sinusoidal mass flow rate. The relatively high frequency, however, produces a dynamic load on the plastic tubing connected to the model. The tube compliance produces a dilatation of its diameter of approximately 1 mm over the ventilation cycle. This in turn causes a deviation of the imposed flow rate, which only approximates a sine wave at the model inlet (Fig. 2). Using completely rigid piping would prevent this effect; but this would not be feasible given the several meters between the MRI scanner and the control room (where the pump is located to shield it from the magnetic field). Past studies indicated that the precise shape of the wave form does not have a qualitatively significant impact on the fluid dynamics (e.g., Ref. [26]), though some effect was recently reported [43].

Table II summarizes the investigated cases in terms of nondimensional numbers. For a given geometry, the Reynolds number is sufficient to characterize the steady cases. This is defined at the trachea as $\text{Re} = U_0 D_0/\nu$, where $D_0 = 4A_0/P_0$ is the hydraulic diameter (A_0 and P_0 being the area and perimeter of the trachea cross section), U_0 is the corresponding bulk velocity, and ν is the kinematic viscosity. The considered trachea cross section is indicated in Fig. 1. Additionally, for the oscillatory flow case, the ventilation frequency is characterized by the Womersley number $\text{Wo} = (D_0/2)\sqrt{\omega/\nu}$ where ω is the angular frequency of the ventilation cycle. The other commonly used parameter is the nondimensional stroke length $2L/D_0 = \text{Re}/\text{Wo}^2$, thus Re and Wo are sufficient to fully characterize the flow regime. The considered steady cases, $\text{Re} = 1500$ and 4500, correspond

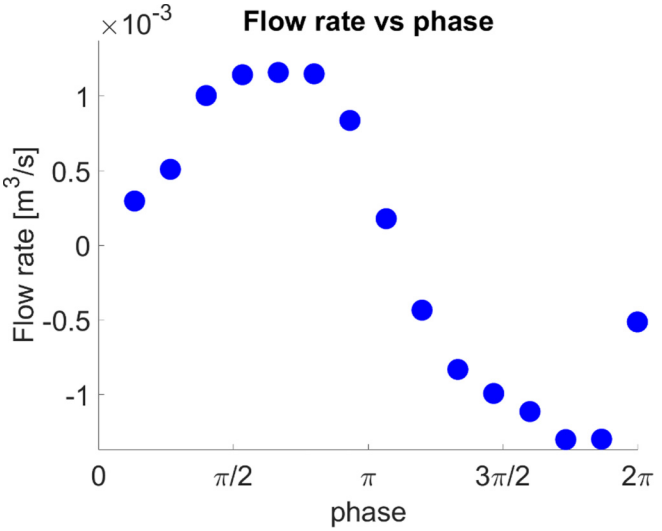

FIG. 2. Flow rate at the model inlet across the ventilation cycle, as measured by MRV.

to breathing air at about 20 and 60 L/min, respectively. The former corresponds to quiet breathing, while the latter is relevant to light exertion or deep inhalation maneuvers. The Reynolds number during steady exhalation, as measured by MRV, is less than 10% lower than in steady inhalation. Significant changes in flow features are not expected due to such difference (also in light of the inhalation results reported below over a much broader range of Re), therefore, in the following both steady cases are nominally labeled as Re = 1500. In the oscillatory case, Wo = 12 corresponds to a ventilation frequency of approximately 5 Hz in an adult, which is in the typical range of clinical HFV applications (as opposed to approximately 0.3 Hz for normal breathing) [26].

In our experiments, we use dynamic similarity to match the physiological nondimensional numbers. This allows us to change physical size and working fluid (in this case, from air to water) as convenient for the MRV measurements; see, e.g., Refs. [20,21,33,34]. The model is scaled down 0.85: 1 from life size, so as to fit in the MRI head coil. The angular frequency imposed by the oscillatory pump is $\omega = 0.7\,\mathrm{rad/s}$.

III. RESULTS

A. Steady regimes

We begin by considering the evolution of the Reynolds number along the bronchial tree. This is defined by the local hydraulic diameter and bulk velocity at each branch cross section. The bulk velocity is the cross-sectional average of the axial velocity U_{ax}. The latter is defined at each voxel as the component parallel to the closest centerline segment, whose orientation is determined via an automatic optimization procedure based on continuity [33]. In Fig. 3(a), we plot the

TABLE II. Reynolds and Womersley numbers for the investigated cases during steady and oscillatory conditions. In the HFV case, the values corresponding to peak inhalation are reported.

	Steady inhalation	Steady exhalation	High frequency ventilation
Re	1500; 4500	1370	1500
Wo			12

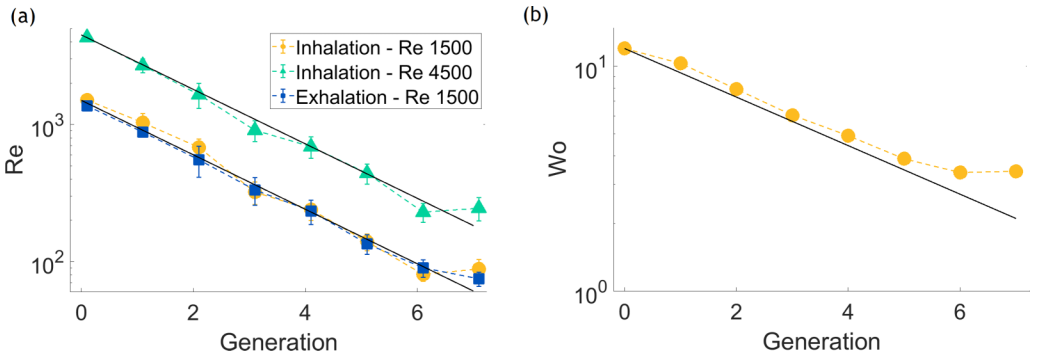

FIG. 3. Reynolds number (a) and Womersley number (b) as a function of generation, for steady and oscillatory cases, respectively. The black lines indicate the theoretical trends according to Eqs. (1) and (2), respectively.

generation-averaged Re values. Here and in the following, error bars represent the standard deviation among the various branches at each generation. In these and in following plots, the generation-averaged quantities are measured along the central 50% of the length of each branch, avoiding the influence of the bifurcation region. Moreover, one should keep in mind that in the expiratory case the flow is from higher to lower generation numbers. The trend follows closely the theoretical behavior expected in a symmetric dichotomous model where the flow rate splits equally between both sibling branches:

$$\mathrm{Re}_{i+1} = \mathrm{Re}_i/2h. \tag{1}$$

Here the subscript indicates the generation number and h is the child-to-parent diameter ratio. The latter is taken as $h = 2^{-1/3} \approx 0.79$ according to the Hess-Murray law that minimizes viscous dissipation [44–46]. We recently found that this value closely predicts actual anatomic proportions in a cohort of 36 subjects, including the present one [33]. In the same study we also showed frequent large asymmetries in the size of sibling branches. Yet, the simple estimate from Eq. (1) appears to predict the trend reasonably well for all steady cases. The averaging, however, hides large local differences between branches (as suggested by the significant standard deviations). These will be discussed later. Similarly, the expected trend for the Womersley number in the oscillatory case is

$$\mathrm{Wo}_{i+1} = \mathrm{Wo}_i/h. \tag{2}$$

Figure 3(b) shows that this is closely reproduced by the measurements, reflecting the fact that the mean diameters approximately follow the Hess-Murray law [33].

Figure 4 also provides information on the axial velocity distribution by displaying, for the steady cases, isosurfaces of $U_{ax} = 0.6^* U_{ax,max}$ (in blue; $U_{ax,max}$ is the maximum axial velocity in the flow field) and $U_{ax} < 0$ (in red). The former represents high momentum regions, which appear to extend deeper in the lower lobes. The latter represents reverse flow region, as the fluid inside those isosurfaces has negative axial velocity. Flow reversal is consequential for gas mixing, particle transport, and mechanotransduction at the epithelium, and was documented for HFV regimes in both idealized and realistic geometries [12,26,47]. Here, pockets of flow reversal appear also in steady conditions, especially at the main bronchial bifurcation. While this is true for both inhalation and exhalation, the position and extent of such pockets are different, and in general they are less prevalent in exhalation. This is consistent with the expiratory velocity profiles being flatter, as will be shown, and so less prone to separation than the inspiratory profiles. In inhalation, the Reynolds number only weakly affects the shape and location of the reverse flow regions, although it increases their size. Compared to the idealized cases, we see large differences in the reverse or

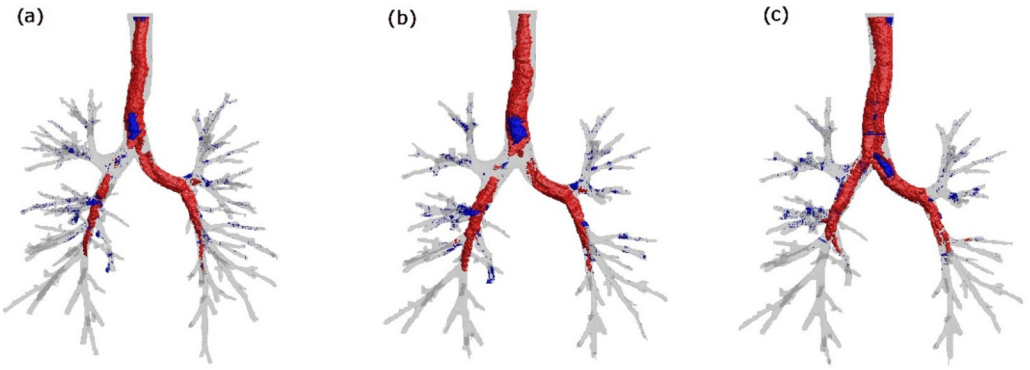

FIG. 4. Isosurfaces of high velocity ($U_{ax} = 0.6^{*}U_{ax,max}$, red) and zero streamwise velocity ($U_{ax} = 0$, blue) along the airway tree for steady inhalation at (a) Re = 1500 and (b) Re = 4500, and (c) exhalation at Re = 1500.

slow flow regions: here they are located above the main bronchial bifurcation, whereas in idealized bifurcations they are found along the external sides [27].

To characterize the profile of axial velocity, we use the momentum distortion parameter D [20], which is a measure of the variation of U_{ax} within each cross section:

$$D = \frac{\int_A (Uax)^2 dA}{Q^2/A} - 1, \tag{3}$$

where A is the cross-sectional area and Q is the local volumetric flow rate. D represents the relative difference between the measured momentum flux and that of a plug flow carrying the same flow rate. It is a measure of axial dispersion due to the mean flow, associated to the amount of longitudinal strain experienced by the fluid at each cross section. In our previous study of an idealized case using a similar methodology, we obtained values of D within 15% of the theoretical value of 0.33 in regions where the flow was expected to approximate a Poiseuille flow [27]. Figure 5(a) shows its evolution of D along the airway tree for the different steady cases. In inhalation, it increases up to the third generation, indicating that the flow velocity profiles become rapidly pointier, and then slowly declines. The close similarity between cases at Re = 1500 and 4500 suggests that this trend is not caused by a transition from turbulent to laminar flow along the tree. It is rather rooted in the propagation of flow features across successive bifurcations, contributing to an increasing skewness of the velocity profiles [27]. The behavior at higher generations is probably affected by the lack of resolution in the smaller branches, where the near-wall fluid layers cannot be captured accurately, and D is in general overestimated. In exhalation, D is generally lower, and it decreases along the flow path. This is due to the exhalation flow profiles being flatter than in inhalation, as illustrated by axial velocity contours in sample locations [Figs. 5(b)–5(d)]. (Here and in the following, the notation Gi refers to the ith branching generation, the mother branch being the zeroth generation.) This trend was noted also in studies focused on idealized geometries [5,12,13]. In turn the more uniform cross-sectional distribution of momentum during exhalation is due to more intense secondary flows, as shown below. The values of D are generally similar to those found in an idealized bifurcation by Jalal and co-workers [12,27].

In order to quantify the secondary flows, which correlate with mixing in the airways [39], we utilize the E parameter [20]:

$$E = \left\{ \frac{\int_A [\vec{u} - (\vec{u} \cdot \hat{n})\hat{n}]^2 dA}{\int_A (\vec{u} \cdot \hat{n})^2 dA} \right\}^{1/2}. \tag{4}$$

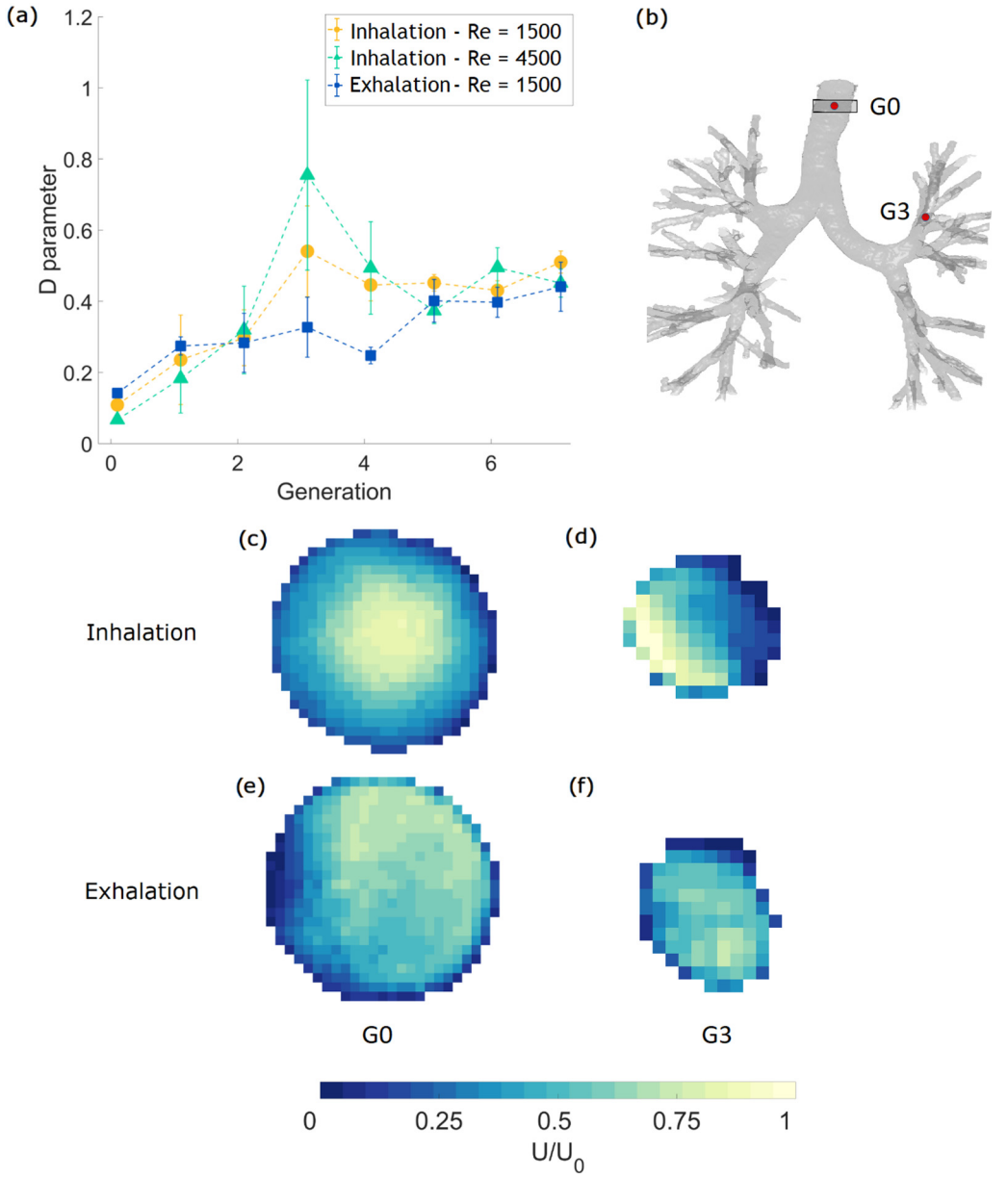

FIG. 5. (a) *D* parameter at all generations for the different steady flow cases. (b) Two selected cross-sections at *G*0 (the trachea) and *G*3, along which normalized axial velocity contours are shown [(c)–(f)].

It represents the relative strength of the secondary velocity compared to the streamwise components over each cross section. We remark that the high-resolution simulations of Bernate *et al.* [48] matched the inspiratory flow MRV measurements of Banko *et al.* [20] to within a few percent of the local velocity values, and their values of the *E* parameters differed from the MRV-based values by less than 15–20% for most considered cross sections. Figure 6(a) shows the evolution of *E* along the branching generations for all steady cases. During inhalation, it increases sharply through the first three generations and plateaus deeper in the bronchial tree, with a marginal effect of Re in the

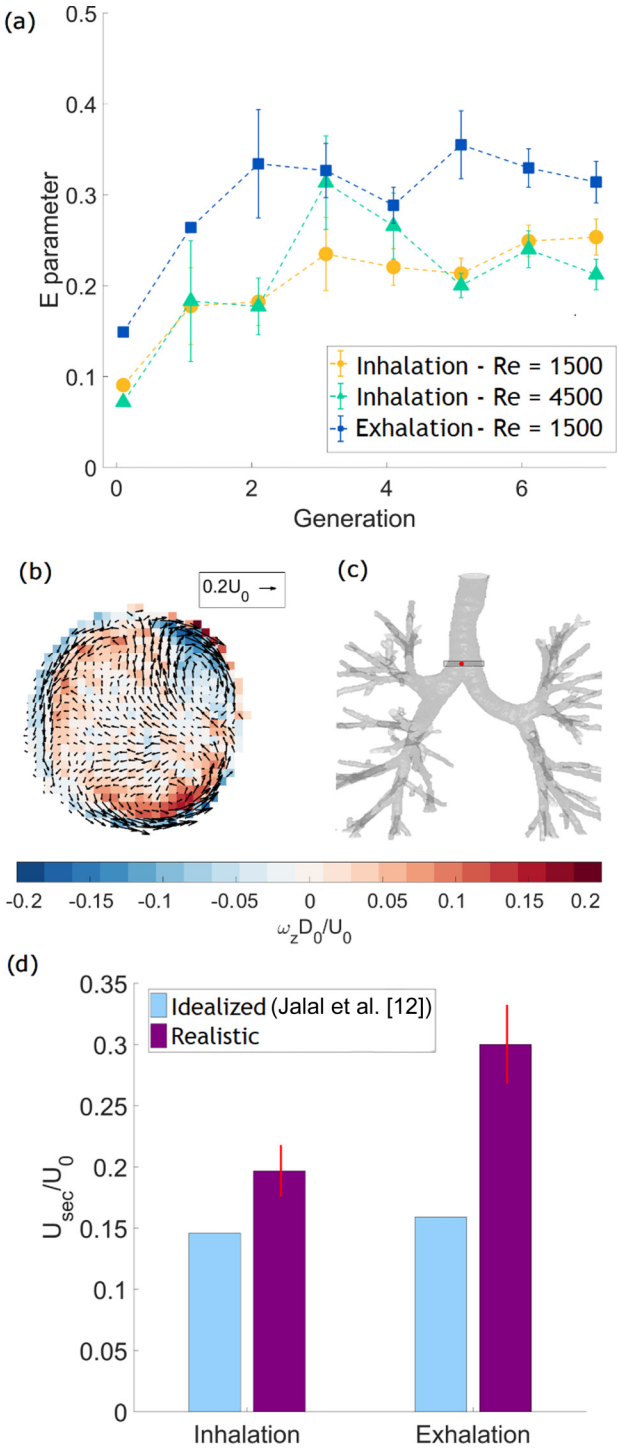

FIG. 6. (a) E parameter at all generations for the different steady flow regimes; (b) cross section with normalized out-of-plane vorticity and in-plane velocity vectors at the location shown in (c) during steady exhalation; (d) normalized secondary flow velocities averaged along $G1$ in the realistic and idealized [12] models at steady inhalation and steady exhalation.

considered range. Secondary flows persist deep in the tree, which is remarkable considering the low values of the local Reynolds number and Dean numbers [20]. During exhalation, E follows a similar trend across the bronchial tree but is significantly higher. This is consistent with the presence of more intense secondary flows caused by the expiratory flow merging at the bronchial junctions and generating more numerous and vigorous streamwise vortices compared to inhalation. At various locations, typically downstream a junction, we recognize the pattern of multiple vortices generated by the interaction of Dean vortices from merging branches; see the sample cross section in Figs. 6(b) and 6(c). This is also found in simple bifurcations [13]. However, the secondary flows in this realistic geometry are even stronger than in idealized bifurcations [12,27]. Figure 6(d) shows the normalized secondary flow velocities U_{sec}/U_0 measured at the first bifurcation in steady inhalation and steady exhalation, compared with the values at the corresponding location in the idealized model of Jalal and co-workers [12,27]. U_{sec} is the cross-sectional average of the secondary velocity component (normal to U_{ax}), and the vertical bars denote the range of variation between right and left bronchus. The secondary flow levels are sizably higher in the realistic airways, especially during exhalation, and the difference between inhalation and exhalation is greatly enhanced.

The increased strength of the secondary motions in the realistic versus idealized model is attributed to a combination of factors related to the airway tree structure. First, compared to the idealized model in Refs. [12,27], the realistic model has naturally curved airways that contribute to strengthening the Dean-type vortices. Second, the average opening angle between sibling branches, which is 60° in Refs. [12,27], here is larger. Van de Moortele *et al.* [30] analyzed the airway morphometry of a cohort of subjects including the present one (with relatively small intersubject variability) and found an opening angle of approximately 90° in the first three generations. Third, unlike the model of Refs. [12,27], the bronchial bifurcations show significant nonplanarity (average rotation angle of 54°; see Ref. [33]). Comer *et al.* [49] compared planar and nonplanar idealized models and showed much stronger secondary flows in the latter. Fourth, and perhaps most importantly, the length-to-diameter ratio in the anatomically accurate model is significantly smaller than the canonical value of 3.5: Van de Moortele *et al.* [33] reported values ranging from 1.5 to 3 in the first five generations. A small airway length contributes to secondary flows propagating across successive generations, counteracting the dissipation of streamwise vortices [27].

As mentioned, the generation-averaged plots, while capturing the ensemble picture, smear the strong local flow variations. To illustrate the latter, in Fig. 7 we plot both D and E parameters along sample paths during steady inhalation and steady exhalation. The normalized abscissa s/D_0 runs along the entire centerline, including the carinal region of the bifurcations. The selected paths in the LUL and LLL are representative of the behavior in the other lobes. Although the global behavior reflects what reported in Figs. 5 and 6, strong local variations are visible. The sharp peaks in the D parameter coincide with the carinal regions, where the streamwise flow is highly nonuniform. Concurrent peaks in the E parameter correspond to locally intense secondary motions, indicating that these are also enhanced at the carinas.

Figure 8 displays spatial distributions of the normalized magnitude of axial and secondary velocity in the entire bronchial tree (down to the resolved generations) under steady inhalation. For illustration, the airway surface is color-coded by the magnitude of U_{ax}/U_0 and U_{sec}/U_0 at the corresponding cross section. The resulting picture points to a strong heterogeneity of both velocity components, beyond the trends indicated by generation averaging. While the axial velocity globally decreases in further generations as expected, there are notable exceptions: there are regions of relatively fast flow deep in the lower lobes, and sudden velocity increases or decreases. In general, the distribution of axial velocity appears very heterogeneous. The spatial changes in secondary velocities are even more abrupt, with sharp differences along bronchial pathways and between sibling branches. The exhalation case shows qualitatively similar trends. Despite some local difference, the $\text{Re} = 1500$ and 4500 cases appear overall similar, confirming that the steady inspiratory topology changes only slightly within the considered range of flow rates.

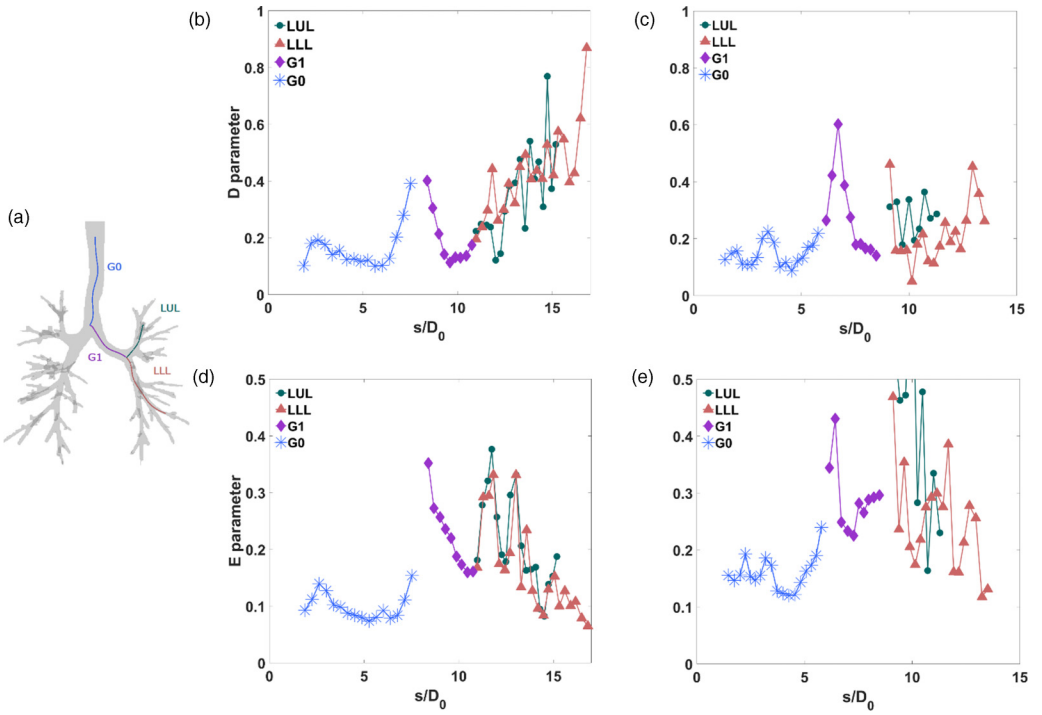

FIG. 7. (b),(c) D parameter and (d),(e) E parameter plotted along (a) selected paths along the bronchial tree for steady inhalation and steady exhalation.

B. Oscillatory regime

1. Streamwise velocity

We begin the study of the HFV regime by observing the distribution of the momentum within the bronchial tree during the various phases of the ventilation cycle. In Fig. 9 we plot isosurfaces of U_{ax} corresponding to 50% of the maximum axial velocity magnitude at each phase, with positive (red) and negative (blue) values associated to inhalation and exhalation, respectively. The 15 panels correspond to the phases resolved in the phase-averaged MRV, numbered according to the abscissa of the plot in Fig. 2. In the exhalation-inhalation and inhalation-exhalation transitions (phase $\phi = 0$ and $\phi = \pi$, respectively), regions of both positive and negative velocities coexist

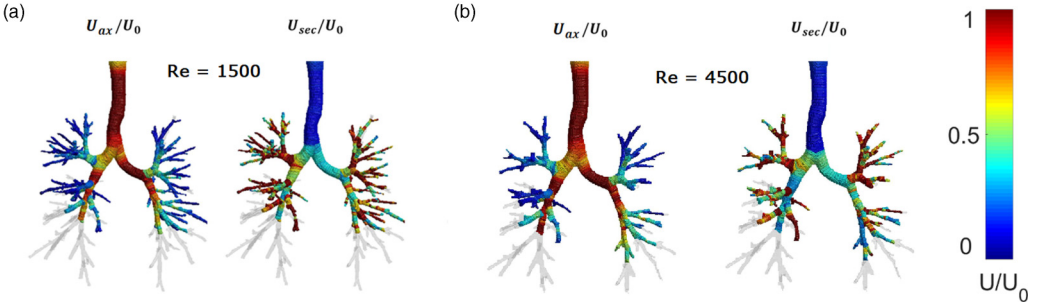

FIG. 8. Normalized magnitude of axial and secondary velocities in the entire bronchial tree under steady inhalation for (a) Re = 1500 and (b) Re = 4500.

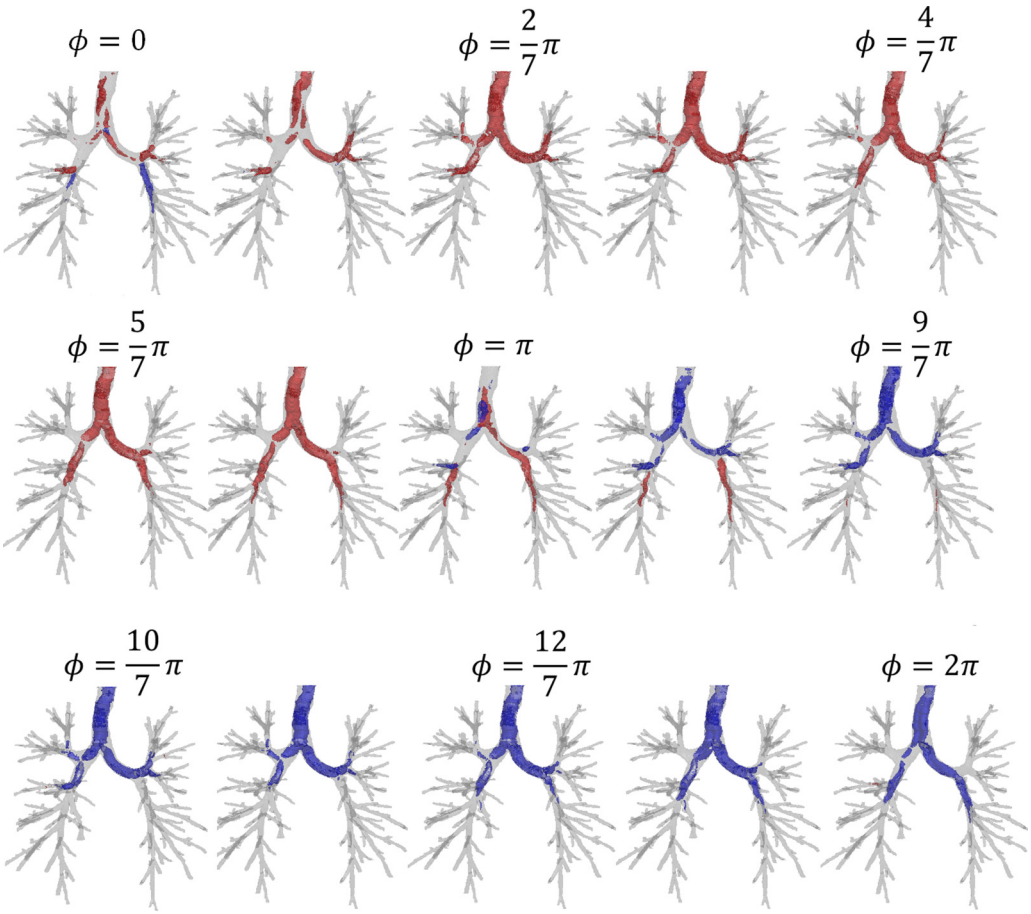

FIG. 9. Velocity isosurfaces for successive phases of the inhalation and exhalation cycle at Wo = 12. Red and blue colors here indicate flow moving in the inspiratory and expiratory direction, respectively, at 50% of the maximum axial velocity.

along the airway tree. Such counterflow regions were documented in both idealized and realistic airway models [12,26,27,38,50]. At the beginning of inhalation (phases $\phi = \frac{1}{7}\pi$ and $\phi = \frac{2}{7}\pi$), high-momentum fluid is found mostly in the trachea and the first two bronchial generations leading to the upper lobes. At peak inhalation and during its deceleration part (phases $\phi = \frac{4}{7}\pi$ to $\phi = \frac{6}{7}\pi$), the high-momentum region shifts towards the branches leading to the lower lobes. Similarly, at the beginning of exhalation, the high momentum regions are prevalently located in the branches leading to the upper lobes; while they are rather found in the lower lobes during the second part of exhalation. The asynchronous behavior of the branches leading to upper and lower lobes, which is specific to HFV, will be discussed in the next subsection.

Figure 10 illustrates counterflow regions at two locations along the trachea, during exhalation-inhalation and inhalation-exhalation transitions. In the straight part of the trachea, the boundary layer along the airway perimeter shows the inversion of flow direction due to phase lag, typical of high-Wo regimes [51]. However, the noncanonical geometry breaks the anterior-posterior symmetry and prevents this feature from clearly appearing in both the transitions phases. Close to the carina, large pockets of reverse flow are observed along the lateral sides of the airway, adjacent to the main bifurcation (hence expansion of the cross section and consequent acceleration or deceleration) where the flow experiences strong streamwise pressure gradients. These features are qualitatively

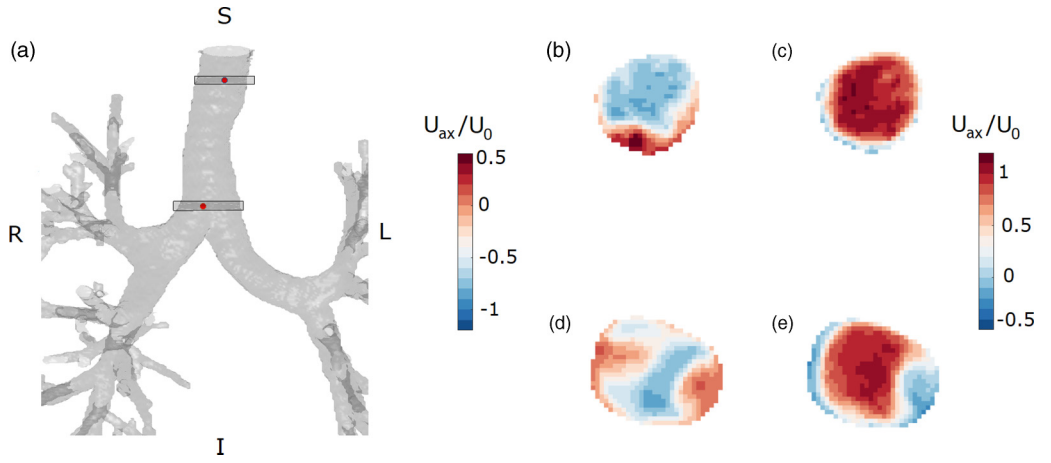

FIG. 10. (a) Locations of two tracheal cross sections taken, and corresponding contour plots of normalized axial velocity during (b),(d) exhalation-inhalation inversion and (c),(e) inhalation-exhalation inversion.

similar to what was observed in the idealized symmetric model at similar Re and Wo [12]. We note that the specific flow topology is expected to be influenced by the upper airways, which are not included in the present model. The potential influence of those on the results is discussed in Sec. IV.

2. Asynchronous flow and pendelluft

The asynchronous behavior of the branches leading to upper and lower lobes is due to unequal mechanical time constants between parallel lung units [52]. At physiological breathing frequencies, the impedance of a bronchial segment is mostly a combination of resistance and compliance. On the other hand, at higher breathing frequencies typical of HFV, the dominant factor becomes the different response of air mass in parallel regions of the lungs to rapid pressure changes [53,54]. Assuming sibling branches have similar diameter, such responsiveness (or inertance) is roughly proportional to the branch length. The upper lobes have visibly shorter branches, which results in lower inertance, hence lower impedance. When an oscillatory ventilation is applied to a bifurcation, the flow rate in the higher-impedance sibling branch will lag the inflow wave form in the parent airway, whereas the lower-impedance branch will anticipate it [55]. This is seen in Fig. 9 and confirmed by Fig. 11, where we plot the flow rate through a bifurcation splitting between LUL and LLL.

The rigid airway replica cannot, by definition, account for the airway compliance. The latter, however, has decreasing impact on the impedance for increasing ventilation frequencies, and therefore can be neglected at the present Wo [54]. The resistance also plays a secondary role at this regime. In our model the resistance is largely determined by the valve setting downstream of the plena, which sets the boundary conditions at peak inhalation-exhalation to match the lobar partition at steady state. If the resistance was a main determinant, then the branches leading to the upper lobes (which receive lower flow rate than the lower lobes; see Table I) would be lagging. Instead, the opposite is observed. This confirms that inertance, which is well captured by our model reproducing the largest branches, dominates over resistance. In conclusion, the deficiencies of our model in capturing the compliance and resistance of a real human bronchial tree, while affecting the quantitative results, do not affect the main conclusions.

The asynchronous flow rate typical of HFV is often reported to cause transfer of mass between adjacent airway segments, also known as *pendelluft* [52,54]. While generally believed to be a crucial mechanism for gas exchange in HFV, pendelluft was rarely observed in simulations of realistic airway trees, and evidence from experimental measurements has been limited to idealized models

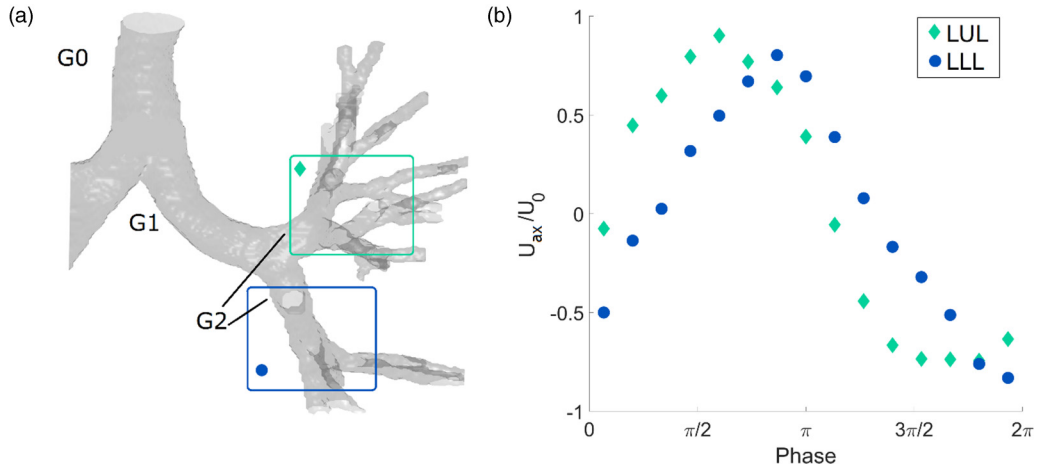

FIG. 11. (a) Selected lobes at *G*2 to highlight (b) the phase lag of axial velocity during the ventilation cycle.

[15,43,50,56–58]. The velocity fields in Fig. 9 suggest that pendelluft is indeed happening around the exhalation-inhalation and exhalation-inhalation transition, with sibling branches simultaneously experiencing opposite flow directions. The specific locations are highlighted in Figs. 12(a) and 12(b), which however only demonstrate "instantaneous" flow patterns.

To verify whether fluid elements are actually transported between sibling branches, a Lagrangian analysis is needed. We therefore leverage the method developed and validated in Ref. [49] to track particles using 3D Eulerian velocity fields. In those studies, the focus was on inertial particles advected by a steady flow; here the approach is applied to massless particles (i.e., tracers) in a time-dependent flow field. The time marching is based on the standard fourth-order Runge-Kutta method in which the time step is specified to keep the particles' displacements within a fraction of the measurement voxel. At each time step, velocity of each particle is updated using a 4D linear interpolation with respect to the structured grid. For further details on the methodology and validation against optical particle tracking, the reader is referred to Ref. [59]. The underlying assumption of the method is that instantaneous velocity fluctuations not captured by MRV have minor impact on the particle trajectories, which is reasonable in the present regime. Figures 12(c) and 12(d) show sample Lagrangian trajectories color-coded according to the phase in the ventilation cycle. The tracers are released from the trachea at peak inhalation. After penetrating into a daughter branch, some tracers do switch to the other sibling branch, providing a direct observation of pendelluft in a realistic airway geometry. Similar paths (not shown) are observed at other locations. Quantifying the relative amount of exchanged fluid at multiple locations would require the integration of a large number of trajectories and is beyond the scope of the present work.

3. Secondary flows

Secondary flows are crucial in the HFV regimes, as they are responsible for lateral dispersion and contribute to strong mixing [60], especially in the transition phases where the streamwise bulk velocity is small. In Fig. 13 we present the normalized secondary velocity U_{sec}/U_0 in the main bronchi (averaged over the branch length) during the ventilation cycle. Steady inhalation and steady exhalation levels are also indicated. We focus on the main bronchi (i.e., the first generation of branches) as this allows for a direct comparison with measurements in the idealized model at a similar regime [12]; other branches in the early generations show similar trends. During the inhalation phase, the secondary flows in both main bronchi are relatively constant and comparable in strength to the steady inspiratory case. During exhalation, the secondary flows quickly grows

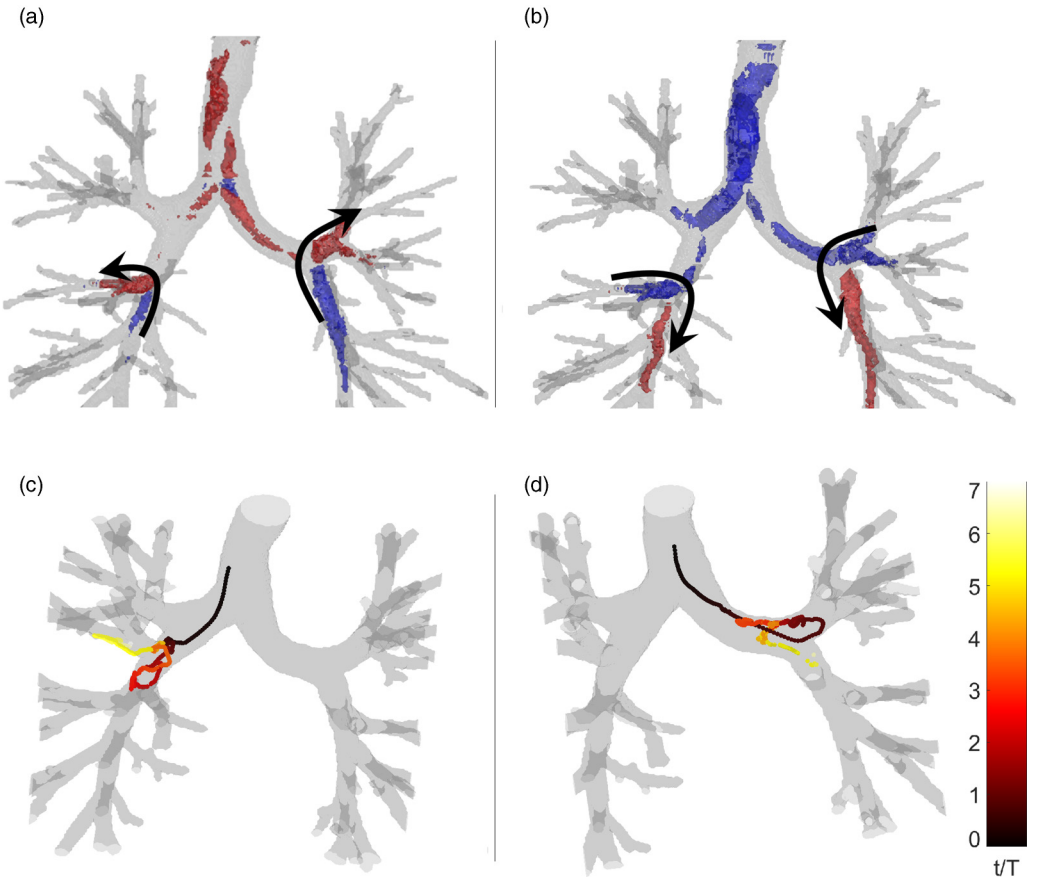

FIG. 12. Asynchronous flow at (a) exhalation-inhalation inversion and (b) inhalation-exhalation inversion; (c),(d) sample Lagrangian trajectories color-coded according to the temporal abscissa t along the ventilation cycle of period T.

in intensity up to a maximum around peak exhalation. The growth is associated to the streamwise vortices merging from the deeper airways into the main bronchi, as we shall discuss. The expiratory secondary flows during HFV reach levels about 50% higher than during inhalation, and comparable to the steady exhalation levels. The secondary motions during both inhalation and exhalation phases are substantially higher than in the idealized case [reported in Fig. 13(b) for comparison], in proportions similar to the steady cases [see Fig. 6(d)]. The reasons are expected to be the same as those behind the secondary flow enhancement in the realistic vs ideal steady case: which is that the realistic bronchi display stronger curvature, larger opening angles, nonplanarity of the bifurcation, and shorter length-to-diameter ratio.

Figure 14 illustrates the secondary flow structures along sample cross sections in the main bronchi, at peak inhalation and peak exhalation. To highlight the streamwise vortices, we use the vortex identifier Γ_2 [61], a scalar quantity defined at any point P [54]:

$$\Gamma_2(P) = \frac{1}{N}\sum_{i=1}^{N} \frac{[PM \times (U_M - \widetilde{U_P})] \cdot z_P}{\|PM\| \cdot \|U_M - \widetilde{U_P}\|}\, dA, \tag{5}$$

where dA is the area of the interrogation window centered on P, N is the number of points M inside the window, and z_P is the unit vector normal to the measurement plane. U_M is the velocity

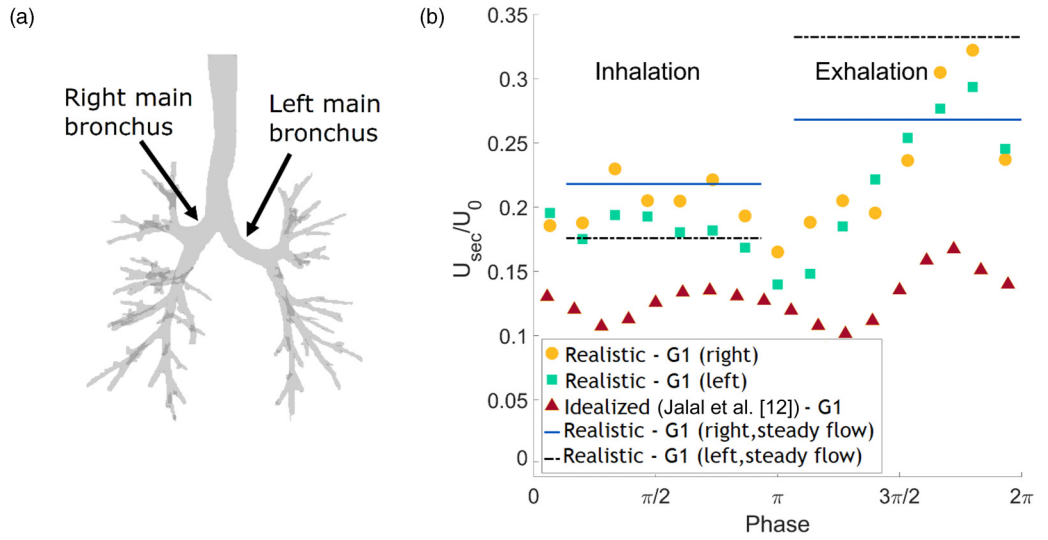

FIG. 13. (a) Location of right and left main bronchi ($G1$) highlighted; (b) normalized secondary velocities averaged along the main bronchi for realistic and idealized [12] airway models. For both cases, the peak Reynolds number and Womersley number are Re = 1500 and Wo = 12, respectively.

vector evaluated at each point M, PM is the vector from P to M and $\widetilde{U_P} = \frac{1}{N}\sum_{i=1}^{N} U\, dA$ is the local convection velocity around P. We choose the radius of interrogation to be 2 voxels (as in Refs. [12,27]). Γ_2 has the same sign as the local out-of-plane vorticity but is more effective at locating rotation-dominated over shear-dominated regions. The flow topology is characterized by multiple vortices, with the expiratory phase showing more numerous vortex cores than the inspiratory phase. This is partly due to the merging of the flow from sibling branches. It is important to note, however, that the mechanisms behind the formation of secondary flows are different and more complex than the steady cases, especially given the relatively large Wo. As recently reviewed and documented in Refs. [62,63], secondary flows in curved ducts under oscillatory regimes are characterized by multiple types of vortical structures, well beyond the Dean vortices found in the steady case. The latter are driven by the imbalance between centrifugal forces and adverse pressure gradients (see Ref. [27] for a detailed description relevant to idealized airway bifurcations). In oscillatory flows other mechanisms become important, due to the rapid acceleration and deceleration

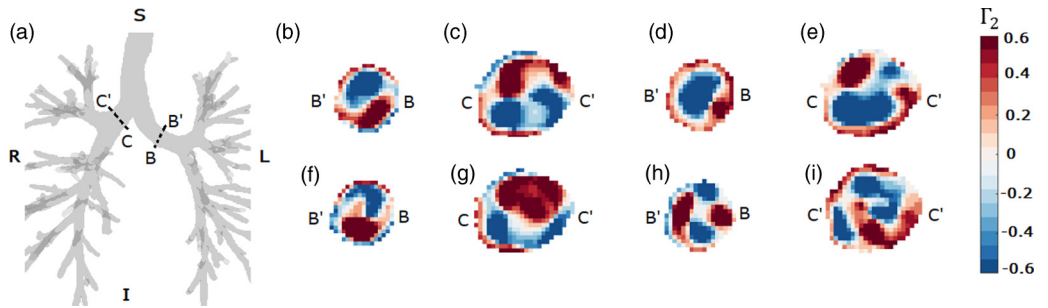

FIG. 14. (a) Locations of selected cross-sections at the main bronchi in HFV conditions; cross sections of Γ_2 at (b),(c) peak inhalation and (d),(e) peak exhalation, compared with (f),(g) steady inhalation and (h),(i) steady exhalation.

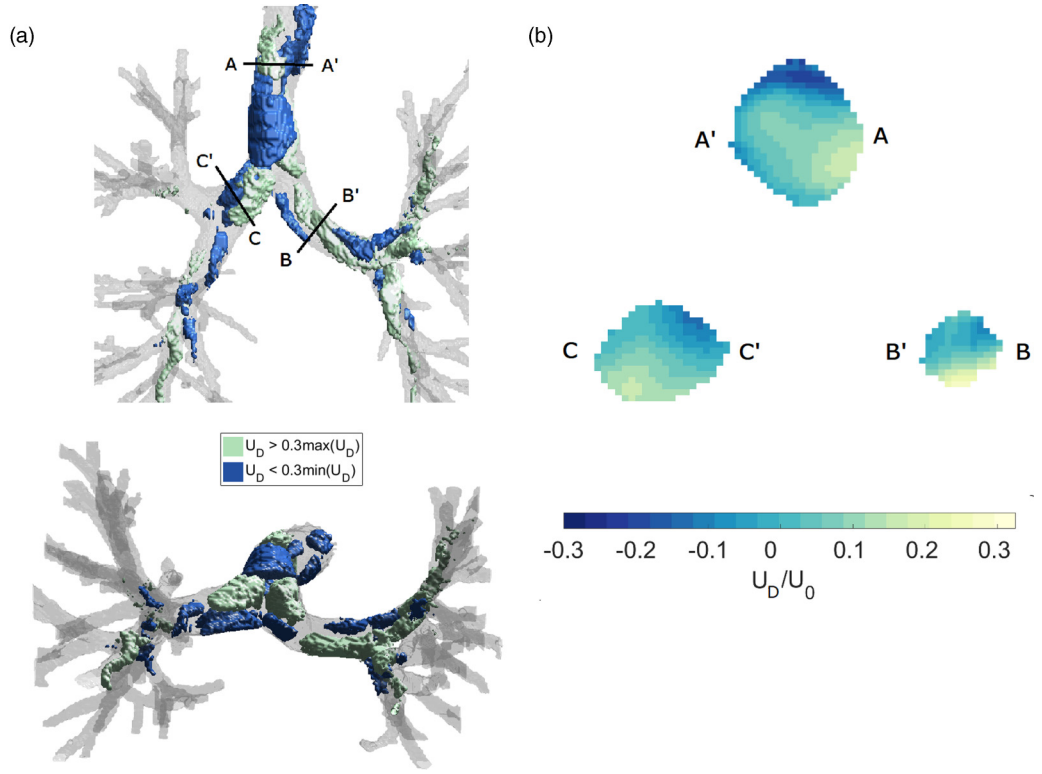

FIG. 15. (a) Isosurfaces of positive-negative drift velocity U_D taken at 30% of the maximum velocity in the domain; (b) contour plots of drift velocity along selected cross sections at the trachea and at the main bronchi.

and give rise to vortices with different location, shape, and sense of rotation compared to the Dean mechanism [62,63]. The formation and topology of the vortex pattern is well known only in idealized (and nonbifurcating) vessels, which might not be directly applicable the present case. Thus, the specific description is outside the scope of the present study. However, it is clear that unsteady effects are key to determine the flow topology in the present regime, although the U_{sec}/U_0 levels are comparable to the steady cases.

4. Steady streaming

It has long been theorized that the asymmetry between the inspiratory and expiratory flow profiles, and the consequent net drift during each respiration cycle (U_D, the cycle average of the streamwise velocity U_{ax}) crucially contributes to the efficient gas exchange in HFV [64–66]. Yet this mechanism, often termed steady streaming, has rarely been documented beyond the mere observation of the asymmetry in the flow profiles [58]. We stress that steady streaming in respiratory flows takes place in very different regimes compared to other fields, such as acoustics, in which the phenomenon can often be modeled as weakly nonlinear. Weak nonlinearity relies on the assumption of small-amplitude oscillations, i.e., $U_0/(\omega D) \sim \mathrm{Re}/\mathrm{Wo}^2 \ll 1$ [67], while in the bronchial tree (e.g., in the present case) $\mathrm{Re}/\mathrm{Wo}^2 = \mathrm{O}(10)$ [14,26]. Thus, simple scaling arguments cannot be applied to predict the magnitude of the streaming velocity. The geometric complexity of the successively bifurcating tree further complicates theoretical predictions: the effect of branch curvature and tapering are superimposed, and the analytical approaches used for both cannot be easily combined [6,68,69]. Experimental or numerical studies are therefore needed; the characterization of the 3D drift velocity in realistic airways, however, has not been achieved

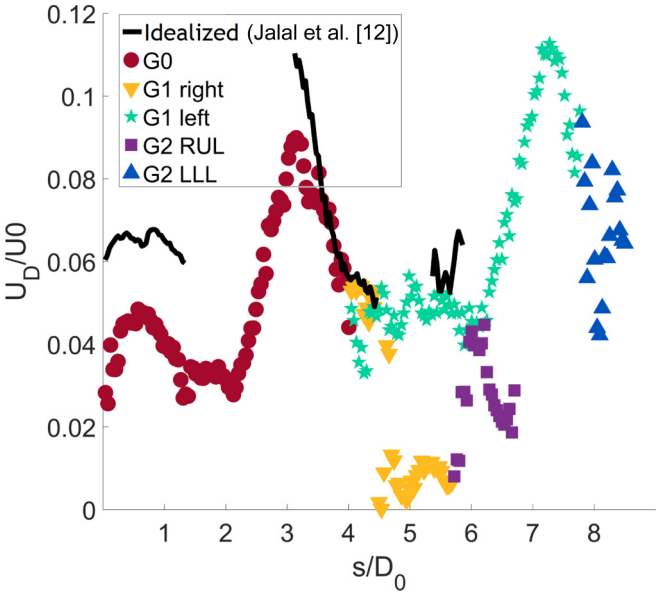

FIG. 16. Magnitude of U_D, (i.e., the cross-section average of its absolute value) normalized by the tracheal bulk velocity U_0, evaluated along two selected bronchial pathways. Both paths start from the trachea ($G0$); one follows the right main bronchus ($G1$ right) and continues in the second generation in the right upper lobe ($G2$ RUL); the other follows the left main bronchus ($G1$ left) and continues in the second generation in the left lower lobe ($G2$ LLL). For comparison, the magnitude of U_D for the idealized model in Ref. [12] is also reported.

experimentally before. Peattie and Schwarz [70] measured the streaming (or drift) velocity U_D, i.e., the cycle average of the streamwise velocity, but they used pointwise velocimetry and could only report on a few linear profiles in a single idealized bifurcation. Bauer and Brucker [50] performed numerical simulations in a more complex and realistic airway tree and could map the full U_D field. They found, however, minimal correlation between steady streaming and ventilation frequency. Jalal *et al.* [12] measured the drift velocity in an idealized model and found its magnitude to be relatively weak and anticorrelated with the ventilation frequency. They explained this finding with the tendency of the flow profiles to be flatter (hence less asymmetric) with increasing Wo. Still, the highly idealized nature of that geometry may have influenced those quantitative results.

With the available 3D and phase-resolved velocity measurements, we carry out an experimental evaluation of steady streaming in realistic airways. As in Ref. [12] we calculate the U_D volumetric field by cycle-averaging U_{ax} at each spatial location. U_D is taken as positive (negative) when directed in inspiratory (expiratory) direction. Figure 15 displays isosurfaces of positive or negative U_D at 30% of the maximum velocity in the domain, as well as contour plots along selected cross sections at the trachea and the main bronchi. Inspiratory drift is prevalent on the anterior side of the main bifurcation, whereas expiratory drift is found on its posterior side. The complex pattern in the main and secondary bifurcations challenges the common view of inspiratory-expiratory drift being located along the internal or external sides of bifurcations [12,64,65]. Clearly the realism and complexity of the tree geometry heavily impacts the streaming flow topology.

In Fig. 16 we plot the magnitude of U_D (i.e., the cross-section average of its absolute value) versus the centerline abscissa, for two different pathways through both main bronchi. For comparison, we also plot the corresponding values calculated with the data from Jalal *et al.* [12] in their two-generation idealized model at similar Re and Wo. Despite the above-mentioned topological differences, the amount of drift and its streamwise evolution is comparable in both the realistic

and idealized cases. An important consideration concerns the contribution of steady streaming to the overall transport. The bulk velocity in each branch is expected to drop by a factor $2h^2$ at each further generation. Thus, we expect (and the measurements confirm) a bulk velocity at peak inhalation-exhalation around $U_0/(2h^2) \approx 0.8U_0$ in the first generation and $U_0/(4h^4) \approx 0.6U_0$ in the second generation. From the magnitude of U_D in Fig. 16, we conclude that steady streaming under the present HFV conditions is much smaller than but not altogether negligible compared to the advective flow. Interestingly, its magnitude does not appear to decrease significantly along the bronchial tree, although the measurement region does not extend deep enough to draw a firm conclusion. Future studies shall clarify how (and whether) steady streaming is correlated with the ventilation frequency in similarly realistic airway trees.

IV. CONCLUSIONS

We have investigated experimentally the three-dimensional flow field in an anatomically accurate replica of the human bronchial tree under various respiratory regimes, imposing physiological and subject-specific boundary conditions. The results are compared with recent studies in a planar double bifurcation of similar proportions. The comparison between cases with different tracheal Re (nominally laminar versus fully turbulent) indicate that the mean flow topology is not significantly affected by the transition to turbulence. In steady exhalation, the secondary motions produced by merging of sibling airways are stronger than those associated to bronchial branching during inhalation. As a result, the expiratory velocity profiles are flatter and the axial dispersion is weaker than their inspiratory counterparts, while the lateral dispersion is more intense. Importantly, these differences between inhalation and exhalation are much larger than previously observed in idealized models. Another noteworthy feature of the flow in the realistic model is the strong heterogeneity. Beyond general trends found in a generation-by-generation analysis, the spatial distribution of axial and lateral velocity is remarkably spotty, especially in the carinal regions. Pockets of slow and even reverse flows are found in the earlier generations, and regions of relatively high velocity can be found deep in the bronchial tree.

Oscillatory flow measurements are carried out at HFV regime and reveal regions of flow reversal during the inhalation-exhalation and exhalation-inhalation transitions. The different impedance (dominated by the inertance) of the various bronchial pathways results in the asynchronous ventilation between the lower and upper lobes. In turn, this leads to pendelluft, which is indicated by Eulerian flow fields and directly demonstrated using Lagrangian path lines. The secondary flow strength at peak inhalation and peak exhalation is similar to that in the corresponding steady cases, although the streamwise vortex pattern can be significantly different, especially for exhalation. The volumetric field of cycle-averaged drifting velocity (so-called steady streaming) is visibly different from the picture gained in idealized airway models: inspiratory-expiratory drift is not strictly associated to the inner or outer side of the bronchial bifurcation, with substantial front-back asymmetry. Contrary to the view that steady streaming is a key transport mechanism in HFV, the drift velocity magnitude appears much smaller than the advective flow, although not altogether negligible and sustained along the first few generations.

This study has several limitations, which however do not detract from its value. For example, the present airway model (as most available CT chest scans) does not include the upper airways. Those are expected to affect the flow in the central airway [32,71], although the intersubject differences observed in the extra-thoracic airways were recently found to largely vanish by the first bifurcation [72]. In particular, the upper airways are inconsequential in several HFV settings, since ventilation is often performed via tracheal tube (e.g., Bauer *et al.* [16]). Additionally, when analyzing the features of a subject-specific model, one cannot capture the variance found in the general population. However, as the considered case is a representative sample of a cohort of 36 subjects displaying consistent airway morphometry [33], the results are believed to have sufficient generality to provide valuable insight.

ACKNOWLEDGMENTS

We gratefully acknowledge the support from the National Science Foundation (Chemical, Bioengineering, Environmental, and Transport Systems, Grant No. 1453538) and the National Institutes of Health (Grants No. NHLBI-R21HL129906 and No. 1S10OD017974-01).

[1] T. Ferkol and D. Schraufnagel, The global burden of respiratory disease, Ann. Am. Thorac. Soc. **11**, 404 (2014).
[2] S. Maio, S. Baldacci, L. Carrozzi, F. Pistelli, A. Angino, M. Simoni, and P. Silvi, Respiratory symptoms/diseases prevalence is still increasing: A 25-yr population study, Respir. Med. **110**, 58 (2016).
[3] C. Kleinstreuer, Z. Zhang, and J. F. Donohue, Targeted drug-aerosol delivery in the human respiratory system, Annu. Rev. Biomed. Eng. **10**, 195 (2008).
[4] P. Das, E. Nof, I. Amirav, S. C. Kassinos, and J. Sznitman, Targeting inhaled aerosol delivery to upper airways in children: Insight from computational fluid dynamics (CFD), PLoS ONE **13**, e0207711 (2018).
[5] T. J. Pedley, Pulmonary fluid dynamics, Annu. Rev. Fluid Mech. **9**, 229 (1977).
[6] J. B. Grotberg, Pulmonary flow and transport phenomena, Annu. Rev. Fluid Mech. **26**, 529 (1994).
[7] J. B. Grotberg, Respiratory fluid mechanics and transport processes, Annu. Rev. Biomed. Eng. **3**, 421 (2001).
[8] C. Kleinstreuer and Z. Zhang, Airflow and particle transport in the human respiratory system, Annu. Rev. Fluid Mech. **42**, 301 (2010).
[9] M. H. Tawhai and C. L. Lin, Image-based modeling of lung structure and function, J. Magn. Reson. Imaging **32**, 1421 (2010).
[10] F. Lizal, D. Stejskal, M. Belka, J. Jedelsky, M. Jicha, K. Brat, and E. L. Sujanska, Variations of flow in human airways as a consequence of lung diseases, in *EPJ Web of Conferences* (EDP Sciences, 2018), Vol. 180, p. 02055.
[11] P. G. Koullapis, P. Hofemeier, J. Sznitman, and S. C. Kassinos, An efficient computational fluid-particle dynamics method to predict deposition in a simplified approximation of the deep lung, Eur. J. Pharm. Sci. **113**, 132 (2018).
[12] S. Jalal, T. Van de Moortele, A. Nemes, O. Amili, and F. Coletti, Three-dimensional steady and oscillatory flow in a double bifurcation airway model, Phys. Rev. Fluids **3**, 103101 (2018).
[13] Y. Zhao and B. B. Lieber, Steady inspiratory flow in a model symmetric bifurcation, J. Biomech. Eng. **116**, 488 (1994).
[14] D. L. Jan, A. H. Shapiro, and R. D. Kamm, Some features of oscillatory flow in a model bifurcation, J. Appl. Physiol. **67**, 147 (1989).
[15] J. M. Drazen, R. D. Kamm, and A. S. Slutsky, High-frequency ventilation, Physiol. Rev. **64**, 505 (1984).
[16] K. Bauer, E. Nof, and J. Sznitman, Revisiting high-frequency oscillatory ventilation in vitro and in silico in neonatal conductive airways, Clin. Biomech. (Bristol, Avon) **66**, 50 (2019).
[17] L. de Rochefort, L. Vial, R. Fodil, X. Maitre, B. Louis, D. Isabey, and G. Sbirlea-Apiou, In vitro validation of computational fluid dynamic simulation in human proximal airways with hyperpolarized 3He magnetic resonance phase-contrast velocimetry, J. Appl. Physiol. **102**, 2012 (2007).
[18] S. Große, W. Schröder, M. Klaas, A. Klöckner, and J. Roggenkamp, Time resolved analysis of steady and oscillating flow in the upper human airways, Exp. Fluids **42**, 955 (2007).
[19] T. Soodt, D. Pott, M. Klaas, and W. Schröder, Analysis of basic flow regimes in a human airway model by stereo-scanning PIV, Exp. Fluids **54**, 1562 (2013).
[20] A. J. Banko, F. Coletti, D. Schiavazzi, C. J. Elkins, and J. K. Eaton, Three-dimensional inspiratory flow in the upper and central human airways, Exp. Fluids **56**, 117 (2015).
[21] A. J. Banko, F. Coletti, C. J. Elkins, and J. K. Eaton, Oscillatory flow in the human airways from the mouth through several bronchial generations, Int. J. Heat Fluid Flow **61**, 45 (2016).

[22] C. J. Elkins and M. T. Alley, Magnetic resonance velocimetry: applications of magnetic resonance imaging in the measurement of fluid motion, Exp. Fluids **43**, 823 (2007).
[23] M. Markl, A. Frydrychowicz, S. Kozerke, M. Hope, and O. Wieben, 4D flow MRI, J. Magn. Reson. Imaging **36**, 1015 (2012).
[24] Z. Zhang and C. Kleinstreuer, Transient airflow structures and particle transport in a sequentially branching lung airway model, Phys. Fluids **14**, 862 (2002).
[25] F. E. Fresconi and A. K. Prasad, Secondary velocity fields in the conducting airways of the human lung, J. Biomech. Eng. **129**, 722 (2007).
[26] J. Choi, G. Xia, M. H. Tawhai, E. A. Hoffman, and C. L. Lin, Numerical study of high-frequency oscillatory air flow and convective mixing in a CT-based human airway model, Ann. Biomed. Eng. **38**, 3550 (2010).
[27] S. Jalal, A. Nemes, T. Van de Moortele, S. Schmitter, and F. Coletti, Three-dimensional inspiratory flow in a double bifurcation airway model, Exp. Fluids **57**, 148 (2016).
[28] E. A. Regan, J. E. Hokanson, J. R. Murphy, B. Make, D. A. Lynch, T. H. Beaty, and J. D. Crapo, Genetic epidemiology of COPD (COPDGene) study design, COPD: J. Chronic Obstruct. Pulm. Dis. **7**, 32 (2011).
[29] G. R. Washko, G. Parraga, and H. O. Coxson, Quantitative pulmonary imaging using computed tomography and magnetic resonance imaging, Respirology **17**, 432 (2012).
[30] J. W. De Backer, W. G. Vos, S. C. Vinchurkar, R. Claes, A. Drollmann, D. Wulfrank, and W. De Backer, Validation of computational fluid dynamics in CT-based airway models with SPECT/CT, Radiology **257**, 854 (2010).
[31] Y. Yin, J. Choi, E. A. Hoffman, M. H. Tawhai, and C. L. Lin, Simulation of pulmonary air flow with a subject-specific boundary condition, J. Biomech. **43**, 2159 (2010).
[32] J. Choi, M. H. Tawhai, E. A. Hoffman, and C. L. Lin, On intra-and intersubject variabilities of airflow in the human lungs, Phys. Fluids **21**, 101901 (2009).
[33] T. Van de Moortele, C. H. Wendt, and F. Coletti, Morphological and functional properties of the conducting human airways investigated by in vivo computed tomography and in vitro MRI, J. Appl. Physiol. **124**, 400 (2018).
[34] T. Van de Moortele, U. Goerke, C. H. Wendt, and F. Coletti, Airway morphology and inspiratory flow features in the early stages of Chronic Obstructive Pulmonary Disease, Clin. Biomech. (Bristol, Avon) **66**, 60 (2019).
[35] M. H. Tawhai, A. J. Pullan, and P. J. Hunter, Generation of an anatomically based three-dimensional model of the conducting airways, Ann. Biomed. Eng. **28**, 793 (2000).
[36] M. H. Tawhai, P. Hunter, J. Tschirren, J. Reinhardt, G. McLennan, and E. A. Hoffman, CT-based geometry analysis and finite element models of the human and ovine bronchial tree, J. Appl. Physiol. **97**, 2310 (2004).
[37] A. Weissheimer, L. M. de Menezes, G. T. Sameshima, R. Enciso, J. Pham, and D. Grauer, Imaging software accuracy for 3-dimensional analysis of the upper airway, Am. J. Orthod. Dentofacial Orthop. **142**, 801 (2012).
[38] P. K. Venuvinod and W. Ma, in *Rapid Prototyping: Laser-based and Other Technologies* (Springer Science & Business Media, New York, 2013), p. 195.
[39] E. M. Cherry, C. J. Elkins, and J. K. Eaton, Geometric sensitivity of three-dimensional separated flows, Int. J. Heat Fluid Flow **29**, 803 (2008).
[40] J. Ohlsson, P. Schlatter, P. F. Fischer, and D. S. Henningson, Direct numerical simulation of separated flow in a three-dimensional diffuser, J. Fluid Mech. **650**, 307 (2010).
[41] O. Amili, D. Schiavazzi, S. Moen, B. Jagadeesan, P. F. Van de Moortele, and F. Coletti, Hemodynamics in a giant intracranial aneurysm characterized by in vitro 4D flow MRI, PLoS ONE **13**, e0188323 (2018).
[42] S. Miyawaki, M. H. Tawhai, E. A. Hoffman, and C. L. Lin, Effect of carrier gas properties on aerosol distribution in a CT-based human airway numerical model, Ann. Biomed. Eng. **40**, 1495 (2012).
[43] M. Alzahrany, A. Banerjee, and G. Salzman, Flow transport and gas mixing during invasive high frequency oscillatory ventilation, Med. Eng. Phys. **36**, 647 (2014).

[44] W. R. Hess, Das prinzip des kleinsten kraftverbrauchs im dienste hämodynamischer Forschung, Archiv fur Anatomie, Physiologie und Wissenschaftliche Medicin **2**, 1 (1913).
[45] C. D. Murray, The physiological principle of minimum work: I. The vascular system and the cost of blood volume, Proc. Natl. Acad. Sci. USA **12**, 207 (1926).
[46] E. R. Weibel, Principles and methods for the morphometric study of the lung and other organs, Lab. Invest. **12**, 131 (1963).
[47] K. B. Heraty, J. G. Laffey, and N. J. Quinlan, Fluid dynamics of gas exchange in high-frequency oscillatory ventilation: In vitro investigations in idealized and anatomically realistic airway bifurcation models, Ann. Biomed. Eng. **36**, 1856 (2008).
[48] J. A. Bernate, T. S. Geisler, S. Padhy, E. S. Shaqfeh, and G. Iaccarino, Study of the flow unsteadiness in the human airway using large eddy simulation, Phys. Rev. Fluids **2**, 083101 (2017).
[49] J. K. Comer, C. Kleinstreuer, and Z. Zhang, Flow structures and particle deposition patterns in double-bifurcation airway models. Part 1. Air flow fields, J. Fluid Mech. **435**, 25 (2001).
[50] K. Bauer and C. Brücker, The influence of airway tree geometry and ventilation frequency on airflow distribution, J. Biomech. Eng. **137**, 081001 (2015).
[51] J. R. Womersley, Method for the calculation of velocity, rate of flow and viscous drag in arteries when the pressure gradient is known, J. Physiol. **127**, 553 (1955).
[52] A. B. Otis, C. B. McKerrow, R. A. Bartlett, J. Mead, M. B. McIlroy, N. J. Selverstone, and E. P. Radford Jr., Mechanical factors in distribution of pulmonary ventilation, J. Appl. Physiol. **8**, 427 (1956).
[53] K. C. High, J. S. Ultman, and S. R. Karl, Mechanically induced pendelluft flow in a model airway bifurcation during high frequency oscillation, ASME J. Biomech. Eng. **113**, 342 (1991).
[54] E. E. Greenblatt, J. P. Butler, J. G. Venegas, and T. Winkler, Pendelluft in the bronchial tree, J. Appl. Physiol. **117**, 979 (2014).
[55] J. S. Ultman, R. G. Shaw, D. C. Fabiano, and K. A. Cooke, Pendelluft and mixing in a single bifurcation lung model during high-frequency oscillation, J. Appl. Physiol. **65**, 146 (1988).
[56] K. Bauer, H. Chaves, and C. Brücker, Visualizing flow partitioning in a model of the upper human lung airways, J. Biomech. Eng. **132**, 031005 (2010).
[57] K. Bauer, A. Rudert, and C. Brücker, Three-dimensional flow patterns in the upper human airways, J. Biomech. Eng. **134**, 071006 (2012).
[58] J. M. Oakes, S. C. Roth, and S. C. Shadden, Airflow simulations in infant, child, and adult pulmonary conducting airways, Ann. Biomed. Eng. **46**, 498 (2018).
[59] O. Amili, R. MacIver, and F. Coletti, MRI-based flow field and Lagrangian particle tracking from a left ventricle assist device, J. Biomech. Eng. **142**, 021007 (2019).
[60] J. J. Fredberg, Augmented diffusion in the airways can support pulmonary gas exchange, J. Appl. Physiol. **49**, 232 (1980).
[61] L. Graftieaux, M. Michard, and N. Grosjean, P. I. V. Combining, POD and vortex identification algorithms for the study of unsteady turbulent swirling flows, Meas. Sci. Technol. **12**, 1422 (2001).
[62] M. W. Plesniak and K. V. Bulusu, Morphology of secondary flows in a curved pipe with pulsatile inflow, J. Fluids Eng. **138**, 101203 (2016).
[63] K. V. Bulusu and M. W. Plesniak, Insights on arterial secondary flow structures and vortex dynamics gained using the MRV technique, Int. J. Heat Fluid Flow **73**, 143 (2018).
[64] F. R. Haselton and P. W. Scherer, Bronchial bifurcations and respiratory mass transport, Science **208**, 69 (1980).
[65] H. K. Chang, Mechanisms of gas transport during ventilation by high-frequency oscillation, J. Appl. Physiol. **56**, 553 (1984).
[66] J. J. Pillow, High-frequency oscillatory ventilation: mechanisms of gas exchange and lung mechanics, Crit. Care Med. **33**, S135 (2005).
[67] N. Riley, Steady streaming, Annu. Rev. Fluid Mech. **33**, 43 (2001).
[68] D. M. Eckmann and J. B. Grotberg, Oscillatory flow and mass transport in a curved tube, J. Fluid Mech. **188**, 509 (1988).
[69] J. B. Grotberg, Volume-cycled oscillatory flow in a tapered channel, J. Fluid Mech. **141**, 249 (1984).

[70] R. A. Peattie and W. Schwarz, Experimental investigation of oscillatory flow through a symmetrically bifurcating tube, ASME J. Biomech. Eng. **120**, 584 (1998).

[71] Y. Feng, J. Zhao, C. Kleinstreuer, Q. Wang, J. Wang, D. H. Wu, and J. Lin, An in silico inter-subject variability study of extra-thoracic morphology effects on inhaled particle transport and deposition, J. Aerosol Sci. **123**, 185 (2018).

[72] P. G. Koullapis, L. Nicolaou, and S. C. Kassinos, In silico assessment of mouth-throat effects on regional deposition in the upper tracheobronchial airways, J. Aerosol Sci. **117**, 164 (2018).